Review of Scientific Instruments

Combining laser interferometry and plasma spectroscopy for spatially resolved high-sensitivity plasma density measurements in discharge capillaries

Cite as: Rev. Sci. Instrum. **92**, 013505 (2021); https://doi.org/10.1063/5.0021117
Submitted: 07 July 2020 • Accepted: 20 December 2020 • Published Online: 11 January 2021

J. M. Garland, G. Tauscher, S. Bohlen, et al.

Review of Scientific Instruments ARTICLE scitation.org/journal/rsi

Combining laser interferometry and plasma spectroscopy for spatially resolved high-sensitivity plasma density measurements in discharge capillaries

Cite as: Rev. Sci. Instrum. 92, 013505 (2021); doi: 10.1063/5.0021117
Submitted: 7 July 2020 • Accepted: 20 December 2020 •
Published Online: 11 January 2021

J. M. Garland,[a] G. Tauscher, S. Bohlen, G. J. Boyle, R. D'Arcy, L. Goldberg, K. Põder, L. Schaper, B. Schmidt, and J. Osterhoff

AFFILIATIONS

Deutsches Elektronen-Synchrotron DESY, Notkestraße 85, 22607 Hamburg, Germany

[a]Author to whom correspondence should be addressed: matthew.james.garland@desy.de

ABSTRACT

Precise characterization and tailoring of the spatial and temporal evolution of plasma density within plasma sources are critical for realizing high-quality accelerated beams in plasma wakefield accelerators. The simultaneous use of two independent diagnostics allowed the temporally and spatially resolved detection of plasma density with unprecedented sensitivity and enabled the characterization of the plasma temperature in discharge capillaries for times later than 0.5 μs after the initiation of the discharge, at which point the plasma is at local thermodynamic equilibrium. A common-path two-color laser interferometer for obtaining the average plasma density with a sensitivity of 2×10^{15} cm^{-2} was developed together with a plasma emission spectrometer for analyzing spectral line broadening profiles with a resolution of 5×10^{15} cm^{-3}. Both diagnostics show good agreement when applying the spectral line broadening analysis methodology of Gigosos and Cardeñoso in the temperature range of 0.5 eV–5.0 eV. For plasma with densities of 0.5–2.5 $\times 10^{17}$ cm^{-3}, temperatures of 1 eV–7 eV were indirectly measured by combining the diagnostic information. Measured longitudinally resolved plasma density profiles exhibit a clear temporal evolution from an initial flat-top to a Gaussian-like shape in the first microseconds as material is ejected out from the capillary. These measurements pave the way for highly detailed parameter tuning in plasma sources for particle accelerators and beam optics.

I. INTRODUCTION

Recent developments in the rapidly evolving area of plasma wakefield accelerator research[1,2] have demonstrated the capability to accelerate electron bunches in cm-scale plasma structures with fields up to the 100 GV m^{-1} level.[3–6] In the blow-out[7] or bubble regime[8]—so-called because of the complete expulsion of electrons from directly behind the wakefield driver—the field produced by the wake can be approximated by the wave-breaking field[9] as $E\ (V\,m^{-1}) \approx 96\ \sqrt{n_0}\ (\mathrm{cm}^{-3})$, where n_0 is the background plasma density. Hence, the forces experienced by charged particle beams are governed by the local plasma density, making the control of the plasma a critical element.

Capillary discharges[10–13] are a common solution for plasma generation in a wakefield accelerator. Such devices are designed to provide specific plasma density profiles in order to generate tailored wakefields,[14] guide laser pulses,[10] and focus particle beams.[15] Tailored longitudinal and radial plasma density profiles can aid in the matching of externally injected charged particle beams, preserving transverse and longitudinal beam quality[16–18] and allowing extended stable wakefield propagation.[19,20] Profile shaping can facilitate the realization of internal injection,[14,21] correction of dephasing,[22] and hosing[23,24] mitigation. Furthermore, the understanding and control of active plasma lenses[15,25]—for the strong focusing of charged particle beams—require precise plasma density profile and temperature knowledge. Hence, it is essential to have a well characterized and controlled plasma profile inside the plasma source.

This paper describes the first measurement of its type in which two complementary plasma diagnostics were used to obtain spatially and temporally resolved plasma-density profiles as well as

spatially averaged and temporally resolved temperature information. A spectrometer for measuring spatially resolved broadening of plasma emission spectra[26] predominantly caused by the Stark effect and a common-path two-color laser interferometer[27,28] for measuring the line-of-sight average plasma density were used in conjunction. By building on previous work by Gigosos and Cardeñoso,[29,30] the temperature-dependent broadening of the hydrogen Balmer-alpha spectral emission line was experimentally calibrated together with the temperature-independent plasma electron density measured by the laser interferometer to yield a temperature characterization. This temperature was subsequently used to obtain highly detailed spatial and temporal electron density characterization from spectral line broadening measurements. The unprecedented sensitivity of these measurements paves the way for detailed studies of the longitudinal plasma density evolution in discharge capillaries, ultimately facilitating much finer control over future applications of plasma sources in particle accelerators.

II. EXPERIMENTAL SETUP

FLASHForward[31,32] is a plasma wakefield experiment based at DESY Hamburg, Germany. The FLASH accelerator[33] provides up to 1.2 GeV electron bunches with micrometer emittance and per-mille energy spread to drive a wakefield in plasma. A capillary discharge is used as the plasma source. At FLASHForward, a plasma characterization experiment has been developed with the aim of obtaining precise temporally and spatially resolved plasma profile information.

Figure 1 shows a schematic of the type of capillary discharge source used at FLASHForward. When equal gas pressure is continually applied to both inlets, a constant neutral gas density profile exists in the central channel.[34] A discharge is initiated via the two electrodes shown at the extremities of the capillary channel. In the main FLASHForward experiment, the electron drive beam (used to create the wakefield) and witness beam (subsequently accelerated by the fields within the wakefield) traverse the main channel along the longitudinal axis.

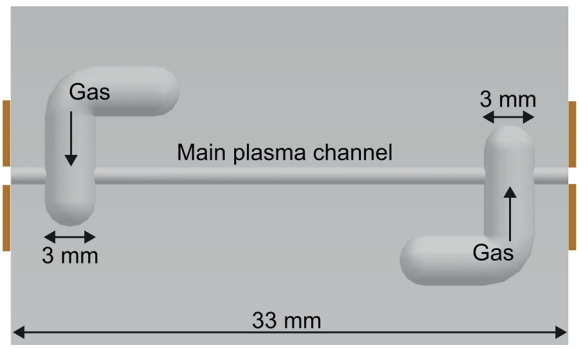

FIG. 1. Schematic of the capillary discharge source used at FLASHForward. The central channel and gas inlets (opposite ends of the main channel) have a circular cross section and are milled from sapphire. The exits of the main channel are open to allow the passage of charged particle beams and lasers. Electrodes with the same diameter opening are placed around these exits. The diameter of the main channel was either 1.0 mm or 1.5 mm. Spontaneous light emission was collected perpendicular to the profile of the sapphire (out of the plane of the image).

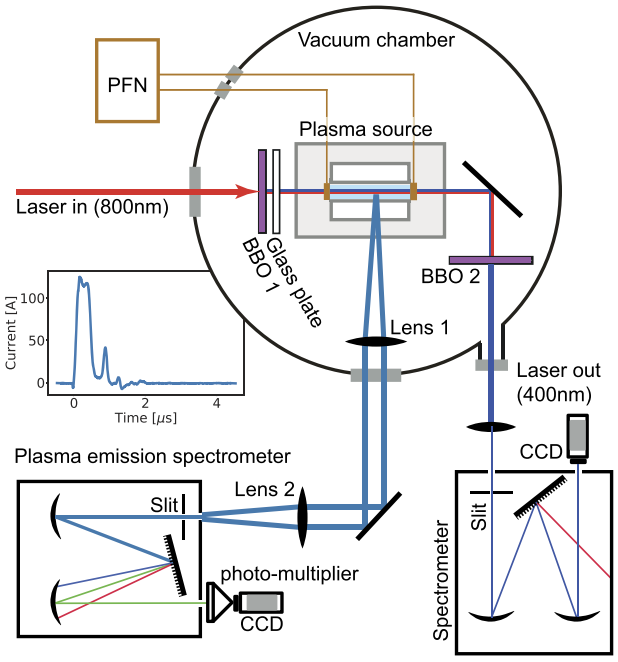

FIG. 2. The experimental setup showing the two diagnostics, viewed from the top. The plasma source is mounted on a stage, allowing movement along the axis of the laser. Spontaneous light emission from the plasma is collected perpendicular to the axis of the capillary channel along which the laser propagates.

In addition to providing a hard-surface environment for the confinement of the plasma, the sapphire material allows the transmission of light emitted during the recombination of the plasma,[35] hence enabling diagnostic spectroscopy. Additionally, the open-ended-capillary geometry facilitates the passage of laser pulses for diagnostic purposes along the longitudinal axis.

A schematic of the experimental plasma characterization setup is shown in Fig. 2. The discharge capillary is mounted within vacuum (1×10^{-6} mbar), and a pulse forming network (PFN) delivers up to 500 A of current in an almost flat-top pulse of 400 ns. The circuit matching impedance was 50 Ω. The voltage used to break down the gas is typically set at 25 kV. Gas is fed into the target via a buffer volume at which location the pressure is measured using a capacitive gauge. Two diagnostics have been developed for plasma characterization in this setup and are described in Secs. III and IV.

III. TWO-COLOR LASER INTERFEROMETER

A common-path two-color laser interferometer (TCI) was deployed to measure the line-of-sight averaged electron density along the center of the capillary channel (see Fig. 2). The fundamental input laser wavelength is 800 nm (titanium–sapphire). The first BBO (beta barium borate) crystal converts around 10% of the incoming laser pulse into a second harmonic copy at 400 nm. A 1 mm glass plate is inserted after the first BBO crystal to generate an initial temporal offset between the pulses (~150 fs). The pulses build up a relative shift during propagation through the plasma due to their different phase and group velocities. After the plasma, another

fraction of the 800 nm pulse is doubled to 400 nm in the second BBO. The two perturbed pulses at the exit of the capillary are imaged onto a 10 μm slit and into a spectrometer (grating 1800 lines/mm blazed at 400 nm) after which a spectral interference pattern is observed on a CCD camera.

Figure 3 shows the phase-axis projection of a set of interferograms in the form of a waterfall plot, indicating the development of the intensity maxima as a function of time as the plasma density evolves during and after the discharge current pulse. The laser spot size was around 0.5 mm in the plasma, and the central ~0.1 mm of the spatial projection of the interferogram was selected for further analysis, corresponding to around 10% of the capillary channel diameter. As the laser was aligned through the center of the capillary, the radial plasma density profile was therefore averaged over 0.1 mm, ±0.05 mm from the longitudinal axis.

The phase shift and spacing of the interference fringes shown in Fig. 3 are dependent on the phase and group velocity of the laser pulse, respectively.[27,28] Although the spacing of the interference fringes was calculated in this work, the contribution was found to be almost negligible in the density range up to 3×10^{17} cm^{-3}. As adequate time resolution was used to determine phase jumps of $> 2\pi$, the contribution from the group velocity dispersion was therefore neglected in this work. Therefore, the dominant phase shift contribution was used to probe the average on-axis plasma density n_e by calculating the integrated phase shift as a function of time,

$$n_e = \frac{4\varepsilon_0 m_e c}{3q_e^2}\frac{\omega_0}{L}\Delta\phi, \tag{1}$$

where ω_0 is the fundamental wavelength of the laser (800 nm), L is the length of the plasma, and $\Delta\phi$ is the total integrated phase shift accumulated during propagation through the plasma.[27,28] The electron mass, charge, speed of light, and vacuum permittivity are given by m_e, q_e, c, and ε_0, respectively.

Figure 4 shows typical measurements of the temporal evolution of the average on-axis plasma density for two different capillaries. The gas used was an argon–hydrogen mixture of 95% and 5% by density, respectively, at a steady-state gas pressure of 20 mbar and

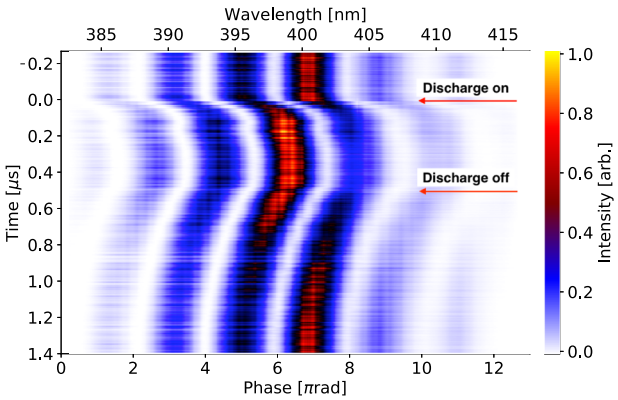

FIG. 3. Evolution of the interference pattern as a function of time during a discharge. Each individual interferogram is projected to the wavelength/phase axis to form one horizontal line in the waterfall plot.

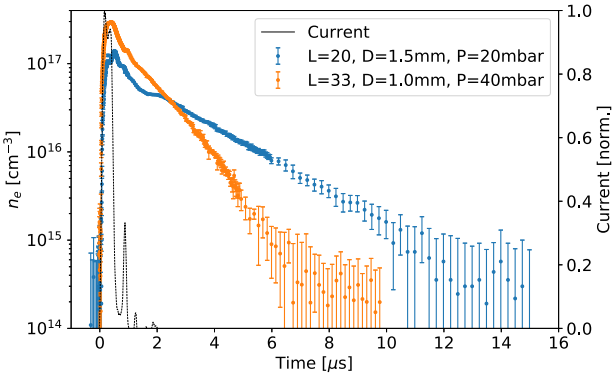

FIG. 4. Measurements using the TCI for capillaries of different lengths (L) and diameters (D) filled with an argon–hydrogen gas mixture at the indicated backing pressures (P). The discharge current profile is indicated by the black curve.

40 mbar, respectively, measured in the buffer volume. The temporal resolution was 2 ns–10 ns, limited mainly by the jitter between the trigger, laser, and discharge, where the jitter between trigger and discharge was the dominant factor. The plasma density resolution was limited by the instrument function of the slit, spectrometer, and camera setup to 2.0×10^{14} cm^{-3}. However, as this technique relies on the integrated effect of the plasma on the laser over the plasma length L, the plasma density sensitivity is a function of L. The sensitivity Φ can be defined as

$$\Phi = \Delta n_e^{min} L, \tag{2}$$

where Δn_e^{min} is the minimum measurable density. The value of Δn_e^{min} for the two capillary lengths shown in Fig. 4 can be estimated by the minimum n_e measured, taking into account the upper error bound. This yields $\Delta n_e^{min} = 1.0 \times 10^{15}$ cm^{-3} and $\Delta n_e^{min} = 0.6 \times 10^{15}$ cm^{-3} for the 20 mm and 33 mm long capillaries, respectively, which leads to a sensitivity of $\Phi = 2.0 \times 10^{15}$ cm^{-2}.

To calculate the density in Fig. 4, the average of the total phase shift over the fixed length of the capillary channel was taken. This neglects the influence of any material ejected from the ends of the capillary along the laser path; however, the diagnostic explicitly records the phase shift contribution from such expulsion. It is assumed that the material ejected in this plume spreads out rapidly in all directions into the surrounding ambient vacuum and the contribution to the line-of-sight integral outside the capillary can be considered negligible. This is supported by the density diagnostic comparison presented in Sec. V.

IV. PLASMA EMISSION SPECTROMETER

A plasma emission spectroscopy imaging diagnostic was developed (see Fig. 2) utilizing spectral line broadening[26] (SLB) to measure the spatially resolved electron density. The spectrometer was a Princeton Instruments SpectraPro 2150i containing a grating with 1200 lines/mm blazed at 500 nm with a spectral range of 50 nm. An Andor iStar DH334T camera was used to capture images. The camera contains an intensified photo-multiplier CCD (iCCD) system with a fast gating time down to 2 ns and a 1024 × 1024 pixel^2 array with a pixel size of 13 μm. This enabled a good temporal

resolution, which was further limited by the signal/noise ratio to around 20 ns in the studies presented here. The optical imaging system and CCD gave a spatial resolution of around 50 μm measured by imaging a micrometer resolution target (R3L3S1N—USAF 1951) placed in the focal plane at the location of the capillary plasma source. The resolution target was also imaged through the capillary wall by placing it in the center, between the sapphire plates. This was realized by disassembling the plasma cell and placing the resolution target behind one of the sapphire plates. This measurement did not reveal a degradation in the resolution caused by the roughness of the capillary surface. It was found that after several tens of thousands of electrical discharge events, the spatial resolution was unaffected. The spectrometer had a spectral resolution of 0.05 nm/pixel; however, the transfer function of the optics and spectrometer setup yields an intrinsic line broadening of 0.7 ± 0.1 nm, making this clearly the largest limiting factor to the spectral resolution.

In the plasma-density range 1×10^{15}–1×10^{18} cm^{-3}, the H_α emission line in the Balmer series exhibits a temperature dependent power-law relationship between SLB and plasma electron density. Hence, small amounts of hydrogen can be added to any gas to provide tracer atoms for density diagnostic purposes. When investigating pure hydrogen, the emission spectrum is typically dominated by the H_α line within the wavelength range of 630 nm–680 nm. However, when analyzing spectra from other gas species doped with hydrogen, great care must be taken to separate the H_α emission line from other spectral lines, which are produced by the primary gas.

In order to identify the background emission lines as the plasma density evolves, a spectrum was first recorded in the plasma formed from pure argon, the primary gas, in the region of the H_α emission line (630 nm–680 nm). Its emission lines were identified, as indicated in Fig. 5(a). This allowed a map to be built up, which could then be used to identify and fit the lines when hydrogen was added. Figure 5(b) shows an example of the emission spectrum recorded in an argon–hydrogen mixture of 95% and 5%, respectively, at the same neutral gas pressure and time after the discharge as in (a).

In the recorded spectra, the background signal is first removed by fitting the spectrum without plasma emission and subtracting this from the recorded signal with plasma emission. Additionally, the contribution from the continuum spectrum of the plasma emission could be removed by fitting a Planck function where the temperature is a free parameter. However, often the continuum contribution was too small to be fitted accurately in this way. When this was the case, a linear fit was made to the continuum background, which was sufficient after ~2μs due to the absence of further heating via the discharge current. Subsequently, all visible peaks above 0.025 of the normalized intensity were fitted with the Faddeeva function,[36] which is a convolution of Gaussian and Lorentzian functions. In each fit, the minimum Gaussian component of the function was set to the instrument function resolution of 0.7 nm. A negligible additional quantity of the Gaussian component was found in the density range investigated in this work; hence, the Doppler broadening component due to a finite temperature did not play a significant role. Other broadening components such as fine structure, van der Waals, and self-absorption were, as expected, not detectable in this work. While some evidence of self-absorption was observed in preliminary studies with pure hydrogen, it was not seen in the argon/hydrogen

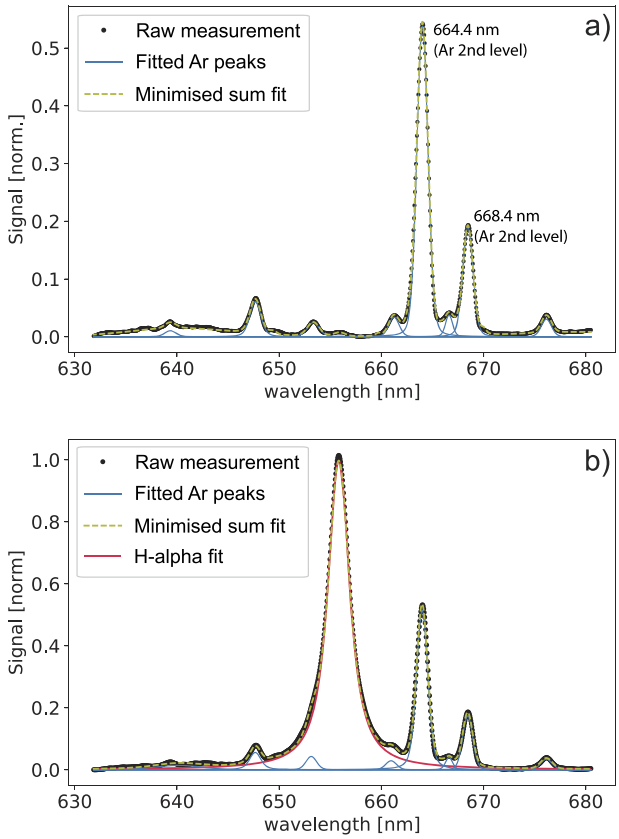

FIG. 5. Example spectra from pure argon (a) and argon doped with 5% hydrogen (b). Measurement data points are shown in black, and individually fitted background argon peaks are shown in blue. The dashed yellow curve in (a) and (b) represents the sum of all fitted peaks with minimized deviation from the measured data. The H_α peak is shown in red in the center of (b) at a wavelength of 656.28 nm. The two larger peaks at 664.37 and 668.43 are due to the second level ionization of argon.

mixture. In addition to the low concentration of hydrogen in the plasmas mainly concerned in this work, this could be due to the relatively low density of the plasma (10^{18} cm^{-3}) and the small line-of-sight distance (0.75 mm) through the plasma that the photons travel before collection. Self-absorption could be a problem if the density of hydrogen is above 10^{18} cm^{-3} in the cell geometry used in this study, for example, when measuring hydrogen-filled capillaries used in laser-plasma wakefield applications, where the electron density is typically of this order. However, in this type of case, self-absorption can be accounted for by measuring emission lines that are less sensitive to the effect, such as the hydrogen Balmer-β line,[37] or by estimating the effect of self-absorption by comparing the emission signal with and without an optical mirror behind the plasma source.[38]

A sum-function of all fitted peaks was then calculated, and a least-squares minimization was used to obtain the best overall sum-fit to the spectrum data (dashed yellow curves in Fig. 5). The full width at half maximum (FWHM) of the Lorentz component of the Feddeeva function $\Delta\lambda(l)$ was then extracted from the fit parameters

of the H_α peak [red curve in Fig. 5(b)] and used to calculate the electron density. The broadening resolution limit is therefore reached when no Lorentz component can be found in the solution to the Feddeeva function, and the total width of the broadened profile is equal to the instrument function broadening. The limit of the fitting residual was set to be <10%, which limited the minimum detectable $\Delta\lambda(l)$ to 0.15 nm equating to an electron density of around 5×10^{15} cm^{-3}. This resolution limit explains why no Doppler broadening component could be resolved in this work. For an electron temperature range of 1 eV–10 eV, the Doppler broadening component at a wavelength of 656.28 nm is 0.05 nm–0.15 nm. As will be shown in Sec. V, the lack of Doppler-broadening is consistent with the measured temperatures.

The imaging system used to collect the plasma light and transport it to the spectrometer is shown in Fig. 2. The center of the capillary was positioned 150 mm from the first lens (focal length 150 mm), and the second lens (also focal length 150 mm) was used to image the center of the capillary channel onto the slit of the spectrometer; the slit opening width was set to 120 μm. The center of the capillary was imaged through the sapphire by setting the second lens position half way between the two points at which each channel-wall extremity was focused. The depth of field was approximately 10 μm. The geometry of the gas inlet regions (see Fig. 1) results in a relative focal plane shift from the central axis of the capillary of up to 300 μm due to the variable sapphire thickness. Hence, the SLB measurement in the gas inlet regions samples a radius of 0 μm < r < 300 μm from the central axis of the capillary, which is important when the radial plasma profile is non-uniform. As the field of view of the imaging system was ~5 mm, 11 measurements along the longitudinal dimension of the capillary were made by moving the plasma source and recombining the data in post-processing.

The upper part of Fig. 6 shows the longitudinally resolved SLB measurement of $\Delta\lambda(l)$ in the 1.0 mm diameter capillary with an argon–hydrogen gas mixture of 95% and 5%, respectively, and a pressure of 40 mbar in the buffer volume for two different times after the initiation of the discharge. The solid curves show the smoothed data using a Savitzky–Golay routine[39] with a second order polynomial fitting. Due to the strong discontinuities around the gas-inlet regions, the Savitzky–Golay smoothing was performed in five different areas independently. The Savitzky–Golay window sizes were 0.5 mm for $0.0 < l < 2.0$ and $31.0 < l < 33.0$ (the channel extremities), 1.0 mm for $2.0 < l < 5.0$ and $28.0 < l < 31.0$ (the gas inlet regions), and 3.0 mm for $5.0 < l < 28.0$ (central part of the channel), where l is the longitudinal position in mm. The effect of the focal plane shift in the gas inlet regions, i.e., the sampling of a different radial position due to the variable sapphire thickness, is most obvious at early times. This effect could not be separated in this work from other dynamic effects such as the expulsion of plasma into the gas inlets. The different characteristics of the plasma in the gas inlet region are strongly affected by the volume of and expansion into the gas delivery channels perpendicular to the central channel (see Fig. 1). The radial plasma density profile has been shown to be parabolic in previous work,[11,35] increasing toward the channel walls. Therefore, neglecting expansion effects, it would be reasonable to assume that the measured density in the gas inlet regions would be higher than in the central channel. As the measured density in the gas inlet regions was lower than in the main channel, it is likely that the expansion of the plasma is the dominant effect. The lower part of

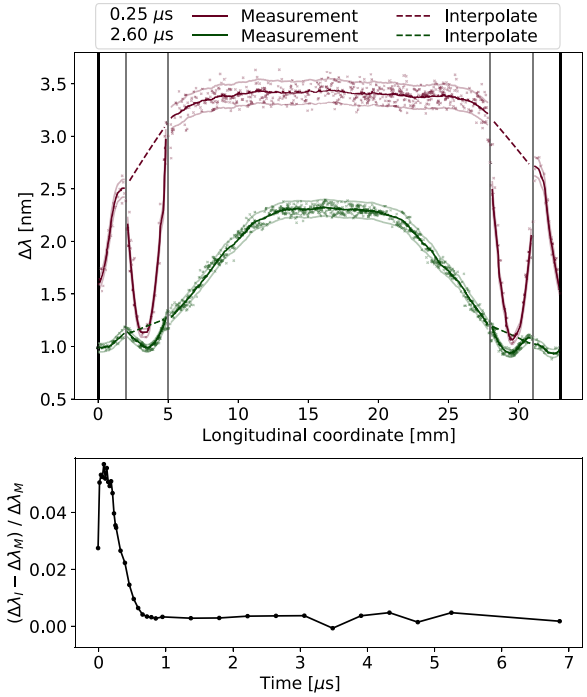

FIG. 6. Red and green points show the longitudinally resolved SLB measurements $\Delta\lambda(l)$ for 0.25 μs and 2.6 μs after the initiation of the discharge, respectively. Each measurement was the average over ten individual measurements at the longitudinal position l. The spatially smoothed (using a Savitzky–Golay routine) average is shown with a bright solid curve, and the upper and lower error bounds (average error on the mean) are indicated by the weaker curves. The gas inlet regions are bounded by gray lines. A straight interpolation of the gas inlet regions is shown with dashed lines. The difference between the longitudinal average of the smoothed curves with ($\Delta\lambda_I$) and without ($\Delta\lambda_M$) interpolation in the gas inlet regions as a function of time is shown in the lower part.

Fig. 6 shows the absolute difference between the longitudinal average SLB measurements, given the different treatment of the gas inlet regions. The value $\Delta\lambda_M$ is the longitudinal average under the measured Savitzky–Golay smoothed curve. The value of $\Delta\lambda_I$ describes the same quantity but with the gas inlet regions replaced by the interpolated (dashed) curve, providing an upper bound. In an argon plasma, it was shown in simulation[40] that after around 350 μs, the radial parabolic density profile in a capillary discharge becomes flatter. Figure 6 shows that the dynamic effects in the gas inlet regions are important in the first 500 μs after the discharge onset but rapidly decrease thereafter. It indicates that the radial profile becomes flatter and closer in magnitude to the channel center over time. The value of $(\Delta\lambda_I - \Delta\lambda_M)/\Delta\lambda_M$ is incorporated into the systematic errors when calculating the longitudinal average of the SLB measurements (see Sec. V).

The methodology developed by Gigosos and Cardeñoso (GC)[29,30] was used to calculate the electron density. Their work combines experimental measurements bench-marked to an extensive set of computer-simulated SLB profiles for different hydrogen emission lines, including H_α. In their work, GC calculated the simulated FWHM of SLB emission profiles $\Delta\lambda(l)$ over a range of plasma densities n_e, plasma temperature T_e, and relative reduced mass μ_r. The

relative reduced mass is defined as

$$\mu_r = \frac{T_e}{T_h}\mu, \tag{3}$$

where T_e and T_h are, respectively, the temperature of the electrons and the heavy ionic and atomic background. The reduced mass μ is defined as

$$\mu = \frac{m_{emit} \cdot m_{pert}}{m_{emit} + m_{pert}}, \tag{4}$$

where m_{emit} is the mass of the emitter particle, i.e., the atom from which the spectroscopic emission is observed, and m_{pert} is the mass of the perturbing particle, i.e., the ionic/atomic background of the plasma. The complete digital dataset for the H_α emission line used in Refs. 29 and 30 was obtained,[41] and a linear 2D interpolation method[42,43] was performed in log-space to connect n_e, $\Delta\lambda(l)$, and T_e for a given μ_r. If three of these four quantities are known, the interpolation can be used to obtain the fourth quantity. For example, if n_e is known from TCI measurements, $\Delta\lambda(l)$ is known from SLB, and μ_r is known simply from knowledge of the gas species, then T_e can be interpolated. As the TCI diagnostic in this work yields the average on-axis plasma density and the SLB diagnostic reveals the spatially resolved broadening along that axis length L, the spatially averaged broadening component was computed as

$$\Delta\lambda_I = 1/L \int \Delta\lambda(l) dl, \tag{5}$$

where $\Delta\lambda(l)$ are the individual spatially resolved SLB measurements at position l in the cell (see Fig. 6).

The dominant error in the measurement of $\Delta\lambda(l)$ and hence n_e is due to the jitter imposed on the iCCD camera trigger signal, resulting from the electromagnetic interference from the discharge current pulse. Small variations in the current pulse result in spurious variations in the trigger signal; hence, the opening window of the intensifier in the iCCD is temporally moved from the intended position.

V. TEMPERATURE MEASUREMENT AND DIAGNOSTIC COMPARISON

The SLB diagnostic was compared to the TCI by computing $\Delta\lambda_I$ from the spatially resolved SLB measurements $\Delta\lambda(l)$, assuming a fixed temperature between $0.5 < T_e < 5.0$, using $\mu_r = 1$ by assuming local thermodynamic equilibrium (LTE), and calculating the electron density using the GC interpolation methodology described above in Sec. IV. The blue shaded region in Fig. 7(a) shows the resulting electron density via the SLB diagnostic when this temperature range is assumed, indicating the potential error due to unknown temperature. This shows that the two diagnostics agree well within the error bars. However, it also shows that by assuming a value of T_e in this range, the error on the electron density n_e could be up to 50% for the SLB diagnostic.

The average on-axis temperature was computed by interpolating the GC dataset, as described above in Sec. IV. The known quantities from measurement were the average on-axis plasma density n_e (TCI measurements), the average on-axis line broadening $\Delta\lambda_I$ (SLB measurements), and $\mu = 1$ for argon gas. Local thermodynamic

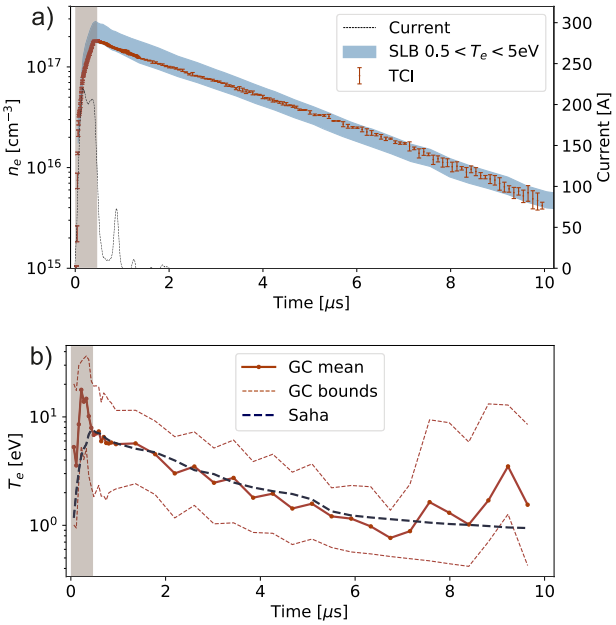

FIG. 7. Longitudinally averaged electron density n_e as a function of time (a) for the TCI (orange points) and the SLB (blue shaded region) diagnostics. The lower n_e bound of the blue shaded region is given by assuming a constant electron temperature $T_e = 5.0$ eV and the upper bound is given by assuming $T_e = 0.5$ eV for the SLB diagnostic. The dashed black curve shows the discharge current profile. Temperature measured via the GC interpolation (b) (orange joined points) and calculated using the Saha equilibrium theory[44] (blue dashed curve). The orange dashed upper and lower limits represent the range of possible temperatures from the GC interpolation, given the errors of the individual measurements of n_e and $\Delta\lambda_I$. The gray shaded region in (a) and (b) represents the time for which the assumption of LTE is not likely to be valid.

equilibrium was assumed. As shown by Sakai *et al.*,[40] the assumption of LTE conditions 0.5 μs after the initiation of the discharge is reasonable. Figure 7(b) shows the resulting temperature T_e for the argon–hydrogen mixture of 95% and 5%, respectively, at a pressure of 40 mbar measured in the buffer volume.

The electron temperature can also be approximated from the TCI electron density measurements via the Saha ionization equations,[44] given that the atomic density n_a is known. However, only the backing pressure in the buffer volume was experimentally known and not the pressure (and thus, atomic density) inside the cell. To approximate n_a, we make the assumption that the maximum of the indirectly measured temperature in the region where LTE is reasonably fulfilled [outside the gray shaded area in Fig. 7(b)] corresponds to the steady-state temperature for the measured peak current. The steady-state MHD (magnetohydrodynamic) formulations of Bobrova, Esaulov, and co-workers[45,46] were solved to yield $n_a = 3.2 \times 10^{16}$ cm^{-3} for the experimental peak current of 220 A and the indirectly measured peak temperature of 7.6 eV. This value is reasonable and compatible with the TCI measurement, considering multiple ionization of argon (supported by the emission spectra as shown in Fig. 5). The blue dashed line in Fig. 7(a) shows the characteristic temperature evolution given by solving the Saha equations and is in good agreement with the indirectly measured temperature.

VI. EVOLUTION OF THE LONGITUDINAL PLASMA DENSITY PROFILE

The value of T_e determined by compiling the temperature dependent SLB measurements with the temperature independent TCI measurements described in Sec. V was used to reduce the uncertainty in the spatially resolved electron density measurements using the SLB diagnostic. To obtain each spatially resolved value of n_e using the SLB, the measured $\Delta\lambda(l)$ was used together with $\mu_r = 1$ and the indirectly measured T_e via the method described in Sec. V and the interpolation of the GC dataset. This method necessitates the assumption of longitudinally uniform temperature due to the longitudinally averaged measurement of n_e from the TCI. The longitudinal plasma density profile along the central axis of a 1.0 mm diameter capillary with the same gas mixture and pressure as in Sec. V was measured. In Fig. 8(a), the longitudinal profile is shown while the current is ramping up (red points), at the beginning of the flat-top of the current pulse (green points), and at the end of the current pulse flat-top (blue points). While the current pulse is present, the plasma density increases rapidly and with a uniform flat-top density profile in the central region due to the initial uniform neutral gas density. The assumption of LTE in this region (0 μs–0.5 μs) is likely to be invalid, leading to an increased systematic error. At early times, the systematic error in this density and temperature range is of the order 1.0^{17} cm^{-3} if $1.0 < \mu_r < 10.0$. As LTE is approached, this error reduces and becomes negligible.

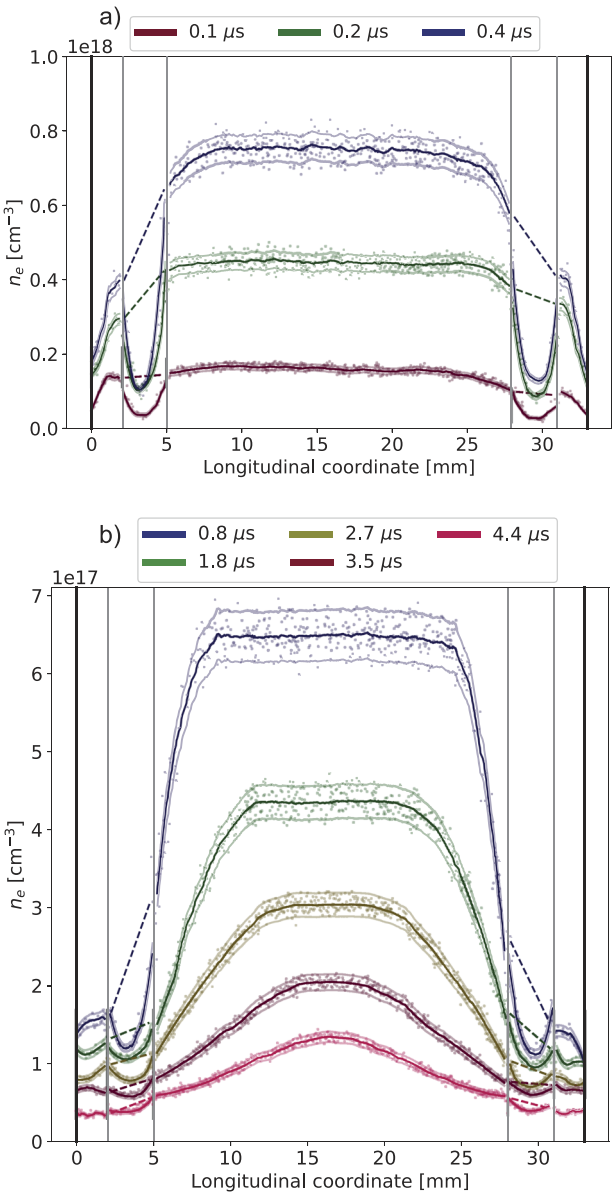

FIG. 8. Longitudinal plasma density profiles at different times during (a) and after (b) the current pulse. The individual points show the average over ten measurements, the Savitzky–Golay smoothing (described in Sec. IV) is shown with a bright solid line, and the upper and lower error bounds are indicated by the weaker lines above and below (95% confidence interval of the error on the mean). The gas inlet regions are bounded by vertical gray lines. The dashed lines show a simple interpolation between the regions either side of the gas inlet.

Figure 8(b) shows the further evolution of the density profile after the current pulse is switched off. The decrease in size of the central flat-top region of the profile due to expulsion of the plasma outward from the open ends of the capillary and into the gas inlet regions is clearly shown as a function of time. The more Gaussian-like profiles shown after 2.5 μs in Fig. 8(b) differ significantly from the often-desired flat-top profile shown in Fig. 8(a).

As already discussed in Sec. IV, the plasma density measured in the gas inlet regions is the result of a complex combination of focal plane shift (thus, radial density variation) and the expulsion of plasma into the gas inlets. Figure 8 indicates that this expansion effect is significant. The difference in electron density between the gas inlet regions and the rest of the capillary becomes smaller with time after the current ceases and the plasma is no longer heated [see Fig. 8(b)]. Ongoing studies are being performed to measure the radial density profile and understand in detail the effect the gas inlets have on the on-axis density profile.

VII. CONCLUSIONS

Two complementary plasma diagnostics were used to characterize the plasma density and temperature in discharge capillaries: a transversely mounted spectrometer for recording broadened plasma emission spectra with a lower density resolution of 5×10^{15} cm^{-3} and a longitudinal common-path two-color laser interferometer with a sensitivity of 2.00×10^{15} cm^{-2}. The TCI was used together with the SLB diagnostic to indirectly measure the average on-axis temperature evolution of the plasma. The temperature exhibits reasonable characteristic behavior that agrees with theory.

The sensitivity of the SLB technique was improved in this work compared to previous studies of plasma density in discharge capillaries. Previous studies were made using spectral broadening techniques in the plasma density range of 10^{18} cm^{-3} to 10^{19} cm^{-3},[47–49] with some reporting lower densities of 10^{17} cm^{-3}.[47] Most such studies were also made with pure hydrogen plasmas and collected spontaneous light emission along the longitudinal capillary axis, as opposed to that perpendicular to it. Together with the higher plasma densities, this increases the likelihood of self-absorption becoming

a problem. This may explain why comparison studies carried out between spectrometry and interferometry in discharge capillaries[50] have exhibited diagnostic disagreement. Typically, in previous studies of discharge capillaries utilizing spectral line broadening, the temperature is simply estimated as roughly 1 eV–3 eV or by assuming that temperature has a negligible effect. However, in this work, the temperature is extracted using the combination of temperature-dependent and -independent plasma diagnostics. This removes the necessity for guesswork or further approximations and allows for the temperature to evolve naturally in time, improving the accuracy of the method.

The importance of measuring the evolution of the longitudinal profile in a discharge capillary plasma source was highlighted. Figure 8 shows that the longitudinal profile evolves from a flat-top to a more Gaussian-like shape during which the extremities of the plasma distribution are expelled from the ends of the plasma source and into the gas inlet regions. This kind of measurement is of utmost importance when considering the beam dynamics in a plasma wakefield accelerator due to the evolution of the density and hence wakefield strength that the beam will experience in its transit through the capillary. With precise knowledge of the longitudinal profile and its temporal evolution, suitable plasma wakefield accelerator parameter choices can be made (for example, at FLASH-Forward, the combination of initial neutral-gas pressure, discharge current and voltage, and the wakefield drive-beam arrival time with respect to a discharge). Tuning these parameters presents the possibility to obtain a specific profile at a given plasma density with suitable entrance and exit ramps to preserve emittance and minimize beam hosing. Such precise characterization will enable better control over injection methods and dephasing for laser- and beam-driven plasma wakefield accelerators.

ACKNOWLEDGMENTS

The authors acknowledge funding from the Helmholtz Matter and Technologies Accelerator Research and Development program and the Helmholtz IuVF ZT-0009 grant. We would like to thank Professor Gigosos for his invaluable help in compiling the data needed to complete the analysis.

DATA AVAILABILITY

The data that support the findings of this study are available from the corresponding author upon reasonable request.

REFERENCES

[1] T. Tajima and J. M. Dawson, Phys. Rev. Lett. **43**, 267 (1979).
[2] P. Chen, J. M. Dawson, R. W. Huff, and T. Katsouleas, Phys. Rev. Lett. **54**, 693 (1985).
[3] I. Blumenfeld, C. E. Clayton, F.-J. Decker, M. J. Hogan, C. Huang, R. Ischebeck, R. Iverson, C. Joshi, T. Katsouleas, N. Kirby *et al.*, Nature **445**, 741 (2007).
[4] A. J. Gonsalves, K. Nakamura, J. Daniels, C. Benedetti, C. Pieronek, T. C. H. de Raadt, S. Steinke, J. H. Bin, S. S. Bulanov, J. van Tilborg *et al.*, Phys. Rev. Lett. **122**, 084801 (2019).
[5] M. Litos, E. Adli, W. An, C. Clarke, C. Clayton, S. Corde, J. Delahaye, R. England, A. Fisher, J. Frederico *et al.*, Nature **515**, 92 (2014).
[6] E. Esarey, C. Schroeder, and W. Leemans, Rev. Mod. Phys. **81**, 1229 (2009).
[7] J. B. Rosenzweig, B. Breizman, T. Katsouleas, and J. J. Su, Phys. Rev. A **44**, R6189 (1991).
[8] A. Pukhov and J. Meyer-ter-Vehn, Appl. Phys. B **74**, 355 (2002).
[9] J. Albritton and P. Koch, Phys. Fluids **18**, 1136 (1975).
[10] A. Butler, D. Spence, and S. M. Hooker, Phys. Rev. Lett. **89**, 185003 (2002).
[11] D. Spence, A. Butler, and S. M. Hooker, J. Opt. Soc. Am. B **20**, 138 (2003).
[12] S. Karsch, J. Osterhoff, A. Popp, T. Rowlands-Rees, Z. Major, M. Fuchs, B. Marx, R. Hörlein, K. Schmid, L. Veisz *et al.*, New J. Phys. **9**, 415 (2007).
[13] W. Leemans, A. Gonsalves, H.-S. Mao, K. Nakamura, C. Benedetti, C. Schroeder, C. Tóth, J. Daniels, D. Mittelberger, S. Bulanov *et al.*, Phys. Rev. Lett. **113**, 245002 (2014).
[14] A. Gonsalves, K. Nakamura, C. Lin, D. Panasenko, S. Shiraishi, T. Sokollik, C. Benedetti, C. Schroeder, C. Geddes, J. Van Tilborg *et al.*, Nat. Phys. **7**, 862 (2011).
[15] C. A. Lindstrøm, E. Adli, G. Boyle, R. Corsini, A. Dyson, W. Farabolini, S. Hooker, M. Meisel, J. Osterhoff, J.-H. Röckemann *et al.*, Phys. Rev. Lett. **121**, 194801 (2018).
[16] K. Marsh, C. Clayton, D. Johnson, C. Huang, C. Joshi, W. Lu, W. Mori, M. Zhou, C. Barnes, F.-J. Decker *et al.*, in *Proceedings of PAC 2005* (IEEE, 2005), pp. 2702–2704.
[17] R. Ariniello, C. Doss, K. Hunt-Stone, J. Cary, and M. Litos, Phys. Rev. Spec. Top.–Accel. Beams **22**, 041304 (2019).
[18] I. Dornmair, K. Floettmann, and A. Maier, Phys. Rev. Spec. Top.–Accel. Beams **18**, 041302 (2015).
[19] Y. Ehrlich, C. Cohen, A. Zigler, J. Krall, P. Sprangle, and E. Esarey, Phys. Rev. Lett. **77**, 4186 (1996).
[20] C. Geddes, C. Toth, J. Van Tilborg, E. Esarey, C. Schroeder, D. Bruhwiler, C. Nieter, J. Cary, and W. Leemans, Nature **431**, 538 (2004).
[21] S. Bulanov, N. Naumova, F. Pegoraro, and J. Sakai, Phys. Rev. E **58**, R5257 (1998).
[22] S. P. Mangles, A. G. R. Thomas, O. Lundh, F. Lindau, M. Kaluza, A. Persson, C.-G. Wahlström, K. Krushelnick, and Z. Najmudin, Phys. Plasmas **14**, 056702 (2007).
[23] D. H. Whittum, W. M. Sharp, S. Y. Simon, M. Lampe, and G. Joyce, Phys. Rev. Lett. **67**, 991 (1991).
[24] T. J. Mehrling, R. Fonseca, A. M. de la Ossa, and J. Vieira, Phys. Rev. Lett. **118**, 174801 (2017).
[25] W. K. H. Panofsky and W. R. Baker, Rev. Sci. Instrum. **21**, 445 (1950).
[26] H. Griem, *Spectral Line Broadening by Plasmas* (Elsevier, 2012).
[27] J. Van Tilborg, A. Gonsalves, E. Esarey, C. Schroeder, and W. Leemans, Opt. Lett. **43**, 2776 (2018).
[28] J. van Tilborg, A. J. Gonsalves, E. Esarey, C. B. Schroeder, and W. P. Leemans, "High-sensitivity plasma density retrieval in a common-path second-harmonic interferometer through simultaneous group and phase velocity measurement," Phys. Plasmas **26**(2), 023106 (2019).
[29] M. A. Gigosos and V. Cardeñoso, J. Phys. B **29**, 4795 (1996).
[30] M. A. Gigosos, M. Á. González, and V. Cardeñoso, Spectrochim. Acta, Part B **58**, 1489 (2003).
[31] A. Aschikhin, C. Behrens, S. Bohlen, J. Dale, N. Delbos, L. Di Lucchio, E. Elsen, J.-H. Erbe, M. Felber, B. Foster *et al.*, Nucl. Instrum. Methods Phys. Res., Sect. A **806**, 175 (2016).
[32] R. D'Arcy, A. Aschikhin, S. Bohlen, G. Boyle, T. Brümmer, J. Chappell, S. Diederichs, B. Foster, M. Garland, L. Goldberg *et al.*, Philos. Trans. R. Soc., A **377**, 20180392 (2019).
[33] K. Tiedtke, A. Azima, N. Von Bargen, L. Bittner, S. Bonfigt, S. Düsterer, B. Faatz, U. Frühling, M. Gensch, C. Gerth *et al.*, New J. Phys. **11**, 023029 (2009).
[34] L. Schaper, L. Goldberg, T. Kleinwächter, J.-P. Schwinkendorf, and J. Osterhoff, Nucl. Instrum. Methods Phys. Res., Sect. A **740**, 208 (2014).
[35] A. Gonsalves, T. Rowlands-Rees, B. Broks, J. Van der Mullen, and S. Hooker, Phys. Rev. Lett. **98**, 025002 (2007).
[36] R. Wells, J. Quant. Spectrosc. Radiat. Transfer **62**, 29 (1999).
[37] M. Ivković, N. Konjević, and Z. Pavlović, J. Quant. Spectrosc. Radiat. Transfer **154**, 1 (2015).

[38]H.-Y. Moon, K. K. Herrera, N. Omenetto, B. W. Smith, and J. D. Winefordner, Spectrochim. Acta, Part B **64**, 702 (2009).
[39]A. Savitzky and M. J. Golay, Anal. Chem. **36**, 1627 (1964).
[40]S. Sakai, T. Higashiguchi, N. Bobrova, P. Sasorov, J. Miyazawa, N. Yugami, Y. Sentoku, and R. Kodama, Rev. Sci. Instrum. **82**, 103509 (2011).
[41]M. A. Gigosos, private communication (2019).
[42]I. Amidror, J. Electr. Imaging **11**, 157 (2002).
[43]MATLAB, 9.7.0.1190202 (R2019b), The MathWorks, Inc., Natick, MA, 2018.
[44]M. R. Zaghloul, M. A. Bourham, and J. M. Doster, J. Phys. D **33**, 977 (2000).
[45]N. Bobrova, A. Esaulov, J.-I. Sakai, P. Sasorov, D. Spence, A. Butler, S. M. Hooker, and S. Bulanov, Phys. Rev. E **65**, 016407 (2001).
[46]A. Esaulov, P. Sasorov, L. Soto, M. Zambra, and J.-I. Sakai, Plasma Phys. Controlled Fusion **43**, 571 (2001).
[47]J. Ashkenazy, R. Kipper, and M. Caner, Phys. Rev. A **43**, 5568 (1991).
[48]N. Edison, P. Young, N. Holmes, R. Lee, N. Woolsey, J. Wark, and W. Blyth, Phys. Rev. E **47**, 1305 (1993).
[49]A. Curcio, F. Bisesto, G. Costa, A. Biagioni, M. Anania, R. Pompili, M. Ferrario, and M. Petrarca, Phys. Rev. E **100**, 053202 (2019).
[50]D. Jang, M. Kim, I. Nam, H. Uhm, and H. Suk, Appl. Phys. Lett. **99**, 141502 (2011).